Grain refinement and superplastic behaviour of a modified 6061 aluminium alloy

R. Kaibyshev, F. Musin, D. Gromov, T. G. Nieh and D. R. Lesuer

The superplastic properties and microstructure evolution of a 0·15%Zr and 0·7%Cu modified 6061 aluminium alloy were examined in tension at temperatures ranging from 475 to 600°C and strain rates ranging from 7×10^{-6} to $2{\cdot}8\times10^{-2}$ s^{-1}. The refined microstructure with an average grain size of about 11 µm was produced in thin sheets by a commercially viable thermomechanical process. It was shown that the modified 6061 alloy exhibits a moderate superplastic elongation of 580% in the entirely solid state at 570°C and $\dot{\varepsilon}=2{\cdot}8\times10^{-4}$ s^{-1}. Superior superplastic properties (elongation to failure of 1300% with a corresponding strain rate sensitivity coefficient *m* of about 0·65) were found at the same strain rate and a temperature of 590°C, which is higher than the incipient melting point of the 6061 alloy (~575°C). The microstructural evolution during superplastic deformation of the 6061 alloy has been studied quantitatively. The presence of a slight amount of liquid phase greatly promotes the superplastic properties of the 6061 alloy, reducing the cavitation level. MST/5315

Professor R. Kaibyshev, F. Musin, and D. Gromov are at the Institute for Metals Superplasticity Problems, Khalturina St. 39, Ufa, 450001, Russia (rustam@anrb.ru). T. G. Nieh and D. R. Lesuer are at the Lawrence Livermore National Laboratory, L-342, PO Box. 808, Livermore, CA 94551, USA. *Manuscript received 27 November 2001; accepted 2 July 2002.*

Introduction

Currently there is great interest in developing new commercial aluminium alloys exhibiting superplastic behaviour. Aluminium alloys with high content of alloying elements usually exhibit excellent superplastic properties. However, these alloys are rather expensive and generally used only for the aerospace industry. The market for superplastic aluminium products is expected to grow, with commercial application of low alloyed aluminium in the automotive, architectural, and construction industries. Inexpensive and weldable aluminium alloys are suitable for these applications. A good candidate for such applications is the 6061 alloy due to its good combination of strength, fatigue resistance and fracture toughness, which have resulted in its wide use as a wrought aluminium alloy. Also, 6061 alloy is heat treatable and can be strengthened appreciably during the paint–bake cycle. The basic requirement for sheets from this material is high formability, which can be provided by making the 6061 Al superplastic.

Several reports have studied the superplasticity of aluminium alloys belonging to the Al–Mg–Si system and produced by ingot metallurgy.[1–3] Commercial 6000 series alloys with standard chemical composition have been demonstrated to exhibit moderate superplastic properties.[1–4] An important current objective is therefore to achieve enhanced superplastic ductilities. The superplastic potential of aluminium alloys is critically dependent upon grain size and its stability during high temperature deformation.[5–7] Minor alloying additives can often enhance grain stability during superplastic deformation to improve superplastic properties.[8] In fact, several aluminium alloys with modified chemical composition have exhibited superplasticity at strain rates that are two or three orders of magnitude faster than those for conventional alloys. Therefore, enhanced superplastic properties can be expected in the 6061 Al through modification of its chemical composition.

In addition, the commercial scale application of 6000 alloys as superplastic materials requires the development of a simple processing route. The phase composition of the 6000 series alloys permits the use of overaging to develop large (~1 µm) secondary precipitates prior to cold rolling.[9,10] During the particle stimulated nucleation (PSN) process, these coarse particles can play a major role in recrystallisation annealing and result in the formation of a uniform fine grained structure for superplasticity.[11,12] However, traditional thermomechanical processing (TMP), consisting of overaging, cold rolling and final recrystallisation annealing, does not produce a fine grain size in a 6000 series alloy because overaging results in plate shaped particles, which do not provide homogeneous nucleation during subsequent recrystallisation.[3,6] To overcome this restriction, a two step overaging/recrystallisation TMP was developed.[3,6] During the first step, the preage rolling and subsequent overaging results in globular precipitates of β-Mg_2Si phase.[3,6] Next, cold rolling and subsequent recrystallisation annealing result in the formation of a structure with an average grain size of about 10 µm.[3,6] However, this TMP is very complicated and difficult to implement in practice.

The present study has two objectives: (i) to enhance superplastic properties of the 6061 aluminium alloy by Zr and Cu additions; (ii) to develop an efficient TMP route for producing a uniform grain structure (~10 µm) suitable for superplastic forming.

Material and experimental procedure

An experimental version of the 6061 alloy with chemical composition Al–1·43Mg–0·5Si–0·7Cu–0·15Zr–0·26Cr–0·14Ti–0·17Fe (wt-%) was manufactured at the Kaiser Aluminium–Center for Technology by direct chill casting. The alloy was solution heat treated at 530°C for 10 h.

The alloy was then subjected to TMP. Hot rolling in the temperature range 400–250°C and cold rolling were carried out using a two high mill with rolls 166 mm in diameter and 200 mm in length. The initial sizes of the specimens for hot and cold rolling were 26 mm × 50 mm × 70 mm and 10 mm × 50 mm × 70 mm, respectively. Following the TMP, tensile samples were machined parallel to the rolling direction with gauge lengths of 12 mm and cross-sectional dimensions of 5 × 3 mm.

Tensile tests were performed at strain rates ranging from 7×10^{-6} to $2{\cdot}8\times10^{-2}$ s^{-1} in the temperature interval

475–600°C. A computer controlled Instron universal testing machine (Model 1185) equipped with a three zone split furnace was used. Temperature accuracy was within ±2 K. The values of the strain rate sensitivity m were determined by strain rate jump tests and calculated as

$$m=\frac{d\ln\sigma}{d\ln\dot{\varepsilon}} \quad . \; . \; . \; . \; . \; . \; . \; . \; . \; . \; . \; . \; . \; . \; . \; . \quad (1)$$

where σ is flow stress and $\dot{\varepsilon}$ is strain rate.[5–7]

Differential thermal analysis was performed on a ~19·7 mg specimen during heating to 630°C at a rate 10 K min^{-1} in air by using a Rigaku analyser (Model Thermoflex).

Samples for metallographic examinations were annealed at $T=165$°C for 4 h in order to decorate grain boundaries with second phase precipitates. These grain boundary particles were then revealed by etching with standard Keller solution. Metallographic analysis was carried out using a Neophot-32 microscope and an Epiquant automated analysis equipment. The average grain size was determined from measurements of more than 400 grains in both longitudinal and transverse directions. Confidence probability in measurements of grain size was calculated as 90%.

Cavitation was measured within the sample body to avoid the effect of surface diffusion. For this purpose, the surface layer of ~0·5 mm thickness was eliminated by mechanical polishing. Central areas of the specimens strained up to $\varepsilon=1{\cdot}1$ and areas of specimens strained up to failure (located 5 mm from the fracture surface) were examined. All samples were strained at a strain rate of $2{\cdot}8\times10^{-4}$ s^{-1}. Metallographic analysis of unetched samples, using the standard point counting technique, was applied to evaluate cavity size and volume fraction of porosity. The average cavity size was determined from measurements of more than 150 voids in both longitudinal and transverse directions to cover the entire cross-section. Confidence probability in measurements of cavity size was calculated as 75%. Cavity aspect ratio CAR was defined as the ratio of the highest dimension of a cavity to that in the perpendicular direction. A mean CAR was defined for each strained sample by measurement of at least 100 cavities. Confidence probability in measurements of CAR was calculated as 70%.

Volume fraction of porosity was concurrently determined by the buoyancy method. For this purpose, samples that were deformed to $\varepsilon=1{\cdot}1$ and pulled up to failure, were cut into segments of 12 mm length. The density of each sample was determined by weighing in air and toluol and calculated as

$$\rho_{\mathrm{S}}=\rho_{\mathrm{T}}\left(\frac{P_{\mathrm{A}}}{P_{\mathrm{A}}-P_{\mathrm{T}}-P_{\mathrm{G}}}\right) \quad . \; . \; . \; . \; . \; . \; . \; . \; . \; . \quad (2)$$

where ρ_s is sample density, P_a is weight of sample in air, P_t is weight of sample in toluol, P_g is weight of sample grip, ρ_t is the theoretical density of toluol of 0·867 g cm^{-3}. Porosity was taken as the ratio

$$V=\frac{\rho-\rho_{\mathrm{S}}}{\rho}\cdot100\% \quad . \; . \; . \; . \; . \; . \; . \; . \; . \; . \; . \; . \; . \quad (3)$$

where ρ is the theoretical density of 6061 Al of 2·7 g cm^{-3} (Ref. 13).

For TEM examinations, samples were thinned to about 0·25 mm. Discs of 3 mm diameter were cut and electropolished to perforation with a Tenupol–3 twinjet polishing unit using a 20% nitric acid solution in methanol at −38°C and 20 V. The thin foils were examined using a Jeol 2000EX TEM with a double tilt stage at an accelerating potential of 160 kV. Energy dispersive X-ray analysis (EDS) of thin foils was carried out to identify second phase particles by using an Oxford attachment (Model Energy TEM200-INCA) to the Jeol 2000EX TEM. Chemical composition was accurate to ±3%. The analysis was done with a focused beam having a diameter of 100 nm positioned on selected dispersoids. At least ten particles of each type were examined to establish their nature. Notably, the beam diameter was usually larger than the size of dispersoids, which results in a higher measured concentration of Al than is actually present.

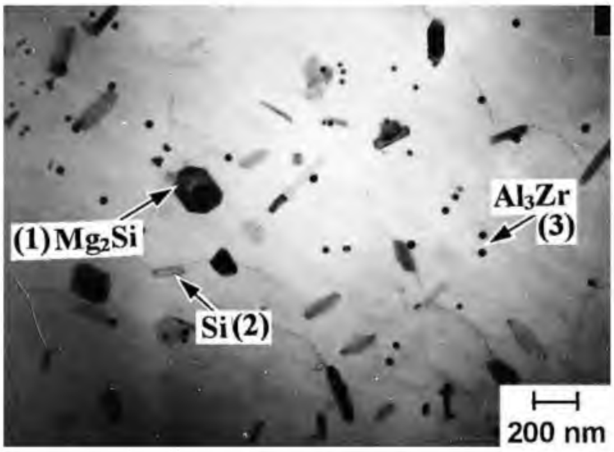

1 Initial microstructure of modified 6061 aluminium alloy after solution treatment at 530°C for 10 h (TEM): typical dispersoids for which chemical composition was determined by EDS technique and represented in Table 1 are indicated

Experimental results

INITIAL MICROSTRUCTURE

Figure 1 shows a typical microstructure of modified 6061 Al after homogenisation. The mean grain size was about 100 μm. Three types of dispersoids with distinct morphology were identified by EDS examination. Particles with square, platelike morphologies having an average size of about 200 nm (dispersoid no. 1 in Fig. 1) had excess magnesium and silicon (Table 1), suggesting that the nature of such particles is Mg_2Si. Particles exhibiting equiaxed or rodlike shape and having an average size of about 100 nm are enriched with Si (dispersoid no. 2 in Fig. 1 and Table 1). Therefore, it is apparent that these dispersoids are elemental Si. Equiaxed dispersoids with sizes ranging from 20 to 80 nm (dispersoid no. 3 in Fig. 1) exhibit increased concentration of zirconium (Table 1), and therefore, the nature of these particles is probably Al_3Zr. It is worth noting that Al_3Zr particles are enriched by silicon (Table 1). As a result, as will be demonstrated below, the volume fraction of Al_3Zr dispersoids is, at least twice as high as that given by the binary phase diagram even assuming that all Zr is present in dispersoids. Al_3Zr dispersoids usually exhibit incoherent boundaries suggesting their stable structure. Al_3Zr dispersoids having a size ~20 nm dominate. No distinct evidence for Al_3Cr type dispersoids was found. It is apparent that after homogenisation Cr is present in solid solution. In addition, α-AlFeSi particles with irregular shape and having a size ~2 μm are present in the initial structure of the modified 6061. Their morphology and size are similar to that in 6061 Al of standard chemical composition.[14]

Table 1 Elemental composition (wt-%/at.-%) of dispersoids indicated in Fig. 1

Dispersoid number	Al	Mg	Si	Zr
1	42·6/42	27·5/30	29·2/27·7	0/0
2	91·9/92·2	0·4/0·44	7·44/7·2	0/0
3	65·6/80	0·47/0·6	8·6/10	24·6/8·9

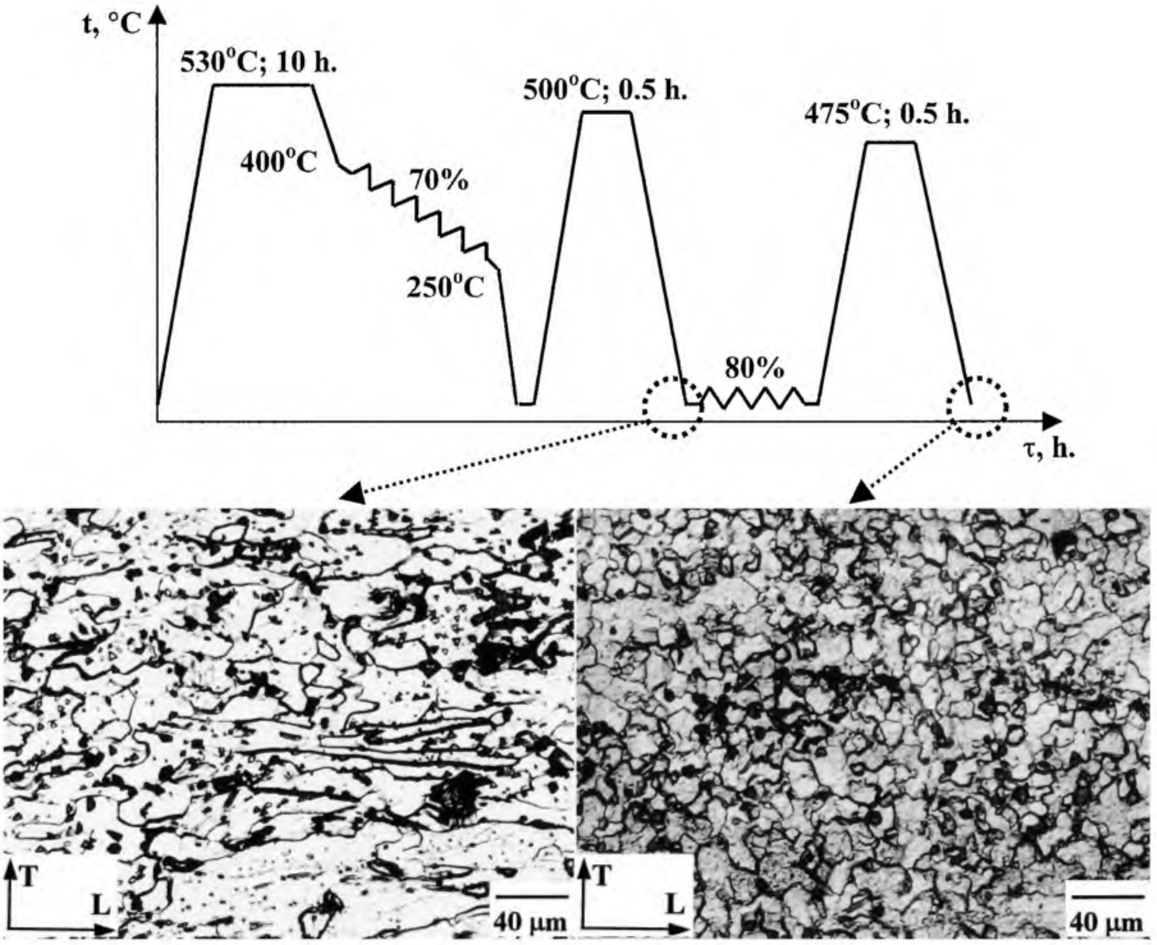

2 **Schematic representation of TMP used to produce fine grained structure in modified 6061 alloy and typical microstructures after first and second steps of TMP**

THERMOMECHANICAL PROCESSING

Recent experiments have shown that it is possible to attain a uniform grain structure by subjecting aluminium alloys to a two step recrystallisation TMP.[15,16] A grain size less than 24 μm prior to the final cold rolling results in homogeneous nucleation and an average grain size of about 10 μm in a number of aluminium alloys during final recrystallisation processing.[15,16] In commercial practice, sheets of the 6061 Al are fabricated by hot rolling of solution treated material, followed by final cold rolling. The two step TMP, which can be a commercially feasible processing route for producing a fine grained structure in modified 6061 Al, consists of the following steps.

(i) The 6061 Al is rolled at a starting temperature of 400°C (the final temperature of the rolled sheet has to exceed 250°C) with a reduction of 70%, followed by recrystallisation annealing in a muffle furnace at 500°C for 30 min

(ii) Next, the 6061 alloy is cold rolled with a reduction of 80%, followed by recrystallisation annealing at a temperature of 475°C in a salt bath for 30 min.

Figure 2 is a schematic representation of this TMP and shows the microstructures developed after each the step. It is seen that the first step of the TMP resulted in a nonuniform structure with an average grain size of ~16 μm (Fig. 2). The proportion of unrecrystallised grains was about 25%. The second step of the TMP resulted in the formation of a uniform microstructure with a mean grain size of 11·2 μm (Fig. 2). Thus, the two step recrystallisation TMP is an effective and simple processing route for obtaining uniform and ultrafine grained structure in modified 6061 Al.

DIFFERENTIAL THERMAL ANALYSIS

Figure 3 shows the DTA curve for the modified 6061 aluminium alloy. It is seen that incipient melting takes place at ~575°C where a weak endothermic reaction occurs. Therefore, the melting temperature for the present 6061 Al is 7 K less than that for the 6061 alloy of standard chemical composition.[13,14,17] Macroscopic melting of the 6061 aluminium starts at 592°C, which is the solidus temperature.

SUPERPLASTIC BEHAVIOUR

The typical true stress–strain curves for the modified 6061 aluminium alloy at an initial strain rate of $\dot{\varepsilon} = 2{\cdot}8 \times 10^{-4}\ s^{-1}$

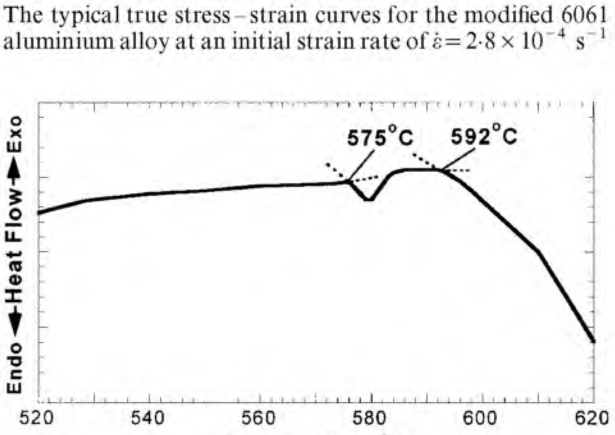

3 **Differential thermal analysis curve for modified 6061 alloy: pointers indicate incipient melting point at 575°C, and 592°C at which extensive melting starts**

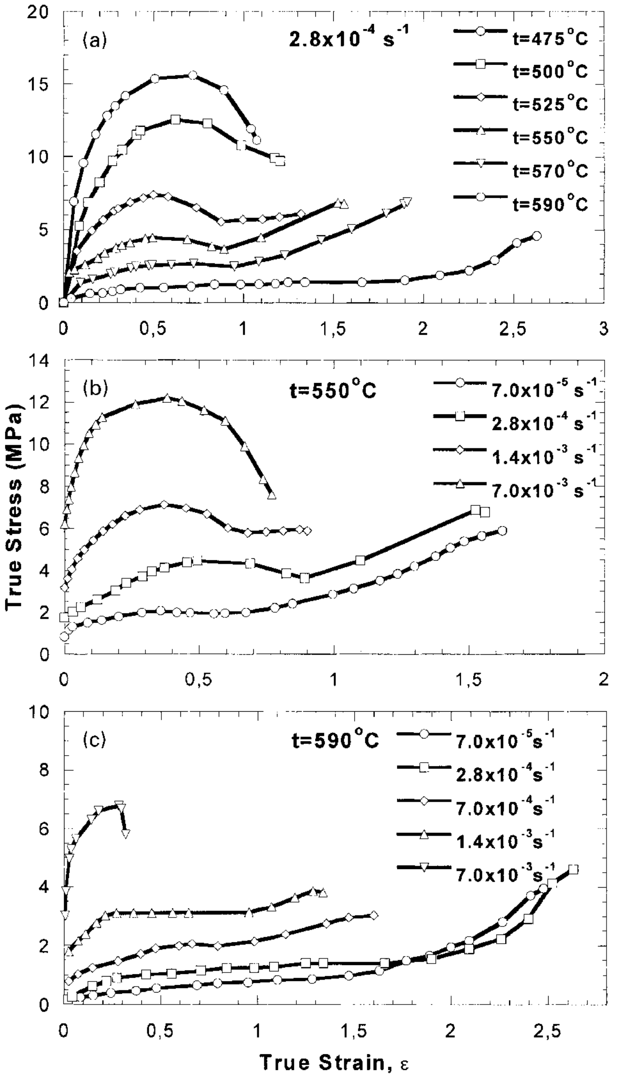

4 ***a*** **effect of temperature on true stress–strain curves at an initial strain rate of $2\cdot8\times10^{-4}$ s^{-1};** ***b*** **and** ***c*** **effect of strain rate on true stress–strain curves at** ***b*** **550°C and** ***c*** **590°C**

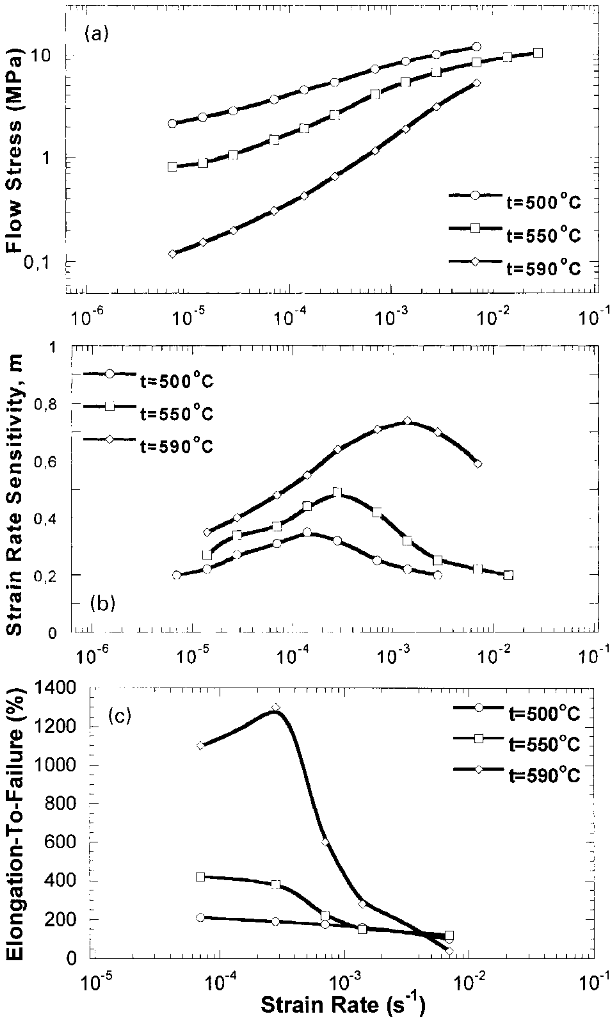

5 Variation of ***a*** **flow stress σ taken at $\varepsilon=0\cdot4$;** ***b*** **coefficient of strain rate sensitivity** ***m*** **taken at $\varepsilon=0\cdot4$;** ***c*** **elongation to failure δ, with strain rate**

and temperatures ranging from 475 to 590°C are shown in Fig. 4*a*. Figures 4*b* and 4*c* shows the $\sigma-\varepsilon$ curves at fixed temperatures of 550°C and 590°C and strain rates ranging from 7×10^{-5} to 7×10^{-3} s^{-1}. The shape of the true stress–strain curves is essentially similar below and above the melting temperature (~575°C). An increase in temperature or a decrease in strain rate results in decreasing flow stress and a reduction in initial work hardening. At low temperature and high strain rates, extensive strain hardening takes place initially. After reaching a maximum stress, the flow stress continuously decreases until failure. A well defined peak in flow stress is observed, and no steady state flow occurs. At high temperatures and low strain rates, apparent steady state flow is attained after a peak stress, and strong secondary strain hardening takes place after the apparent steady state flow. Increasing temperature leads to a reduction in primary strain hardening. At $T\geqslant590$°C, no peak stress was observed at $\dot{\varepsilon}\leqslant1\cdot4\times10^{-3}$ s^{-1}. At $\dot{\varepsilon}\geqslant2\cdot8\times10^{-4}$ s^{-1}, decreasing strain rate results in a shift of the onset of the secondary hardening stage towards higher strains; at lower strain rate, the onset of the secondary hardening stage shifts towards lower strain.

Figure 5 shows plots of flow stresses taken at a true strain of 0·4 (except $\dot{\varepsilon}=7\times10^{-3}$ s^{-1} at 590°C where a strain of 0·3 was used), the coefficient of strain rate sensitivity m and elongation to failure δ as functions of initial strain rate. It is seen that below the incipient melting point (~575°C), the $\sigma-\dot{\varepsilon}$ curves show evidence of a sigmoidal shape with the maximum strain rate sensitivity coefficient m at strain rates slightly above 10^{-4} s^{-1}. However, the highest superplastic ductilities are observed at the lowest strain rate. At 590°C, a well defined maximum elongation to failure of 1300% takes place at $\dot{\varepsilon}=2\cdot8\times10^{-4}$ s^{-1} with the corresponding $m=0\cdot65$. At the same time, the highest m value (0·74) was found at a higher strain rate of $1\cdot4\times10^{-3}$ s^{-1}, at which $\delta=280\%$. Increasing temperature results in expanding the strain rate ranges for superplasticity (distinguished by $m\geqslant0\cdot33$) from $2\cdot8\times10^{-5}-1\cdot4\times10^{-3}$ s^{-1} at 550°C, to $1\cdot4\times10^{-5}-7\times10^{-3}$ s^{-1} at 590°C (Fig. 5*a* and *b*), and increasing δ and m values (Fig. 6). At $\dot{\varepsilon}=2\cdot8\times10^{-4}$ s^{-1}, the sharp increase in δ value from 580% to 1300% occurs with an increase in temperature from 570 to 590°C and can be associated with partial melting at 575°C (Fig. 6). However, at $\dot{\varepsilon}=7\times10^{-3}$ s^{-1}, the partial melting results in reduced ductility (Fig. 5*c*). At 590°C the superplastic properties are superior only at strain rates lower than $1\cdot4\times10^{-3}$ s^{-1}, and at higher strain rates, the elongation to failure is less than that at the lower temperatures despite increased m values (Fig. 5). At 600°C, a highly reduced δ value is observed, in spite of the fact that the m value approaches unity (Fig. 6). Failure occurs with limited plastic flow ($\delta=15\%$) because of the presence of massive liquid phase, since extensive melting takes place at ~592°C.

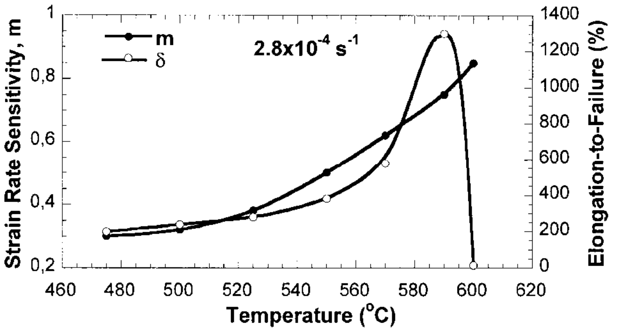

6 Elongation to failure δ and coefficient of strain rate sensitivity m as functions of temperature at $\dot{\varepsilon}=2{\cdot}8\times10^{-4}$ s^{-1}

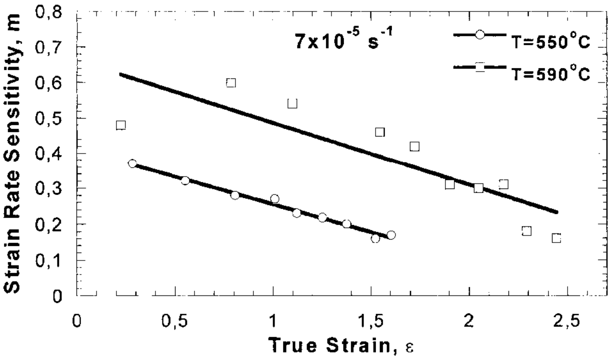

7 Effect of strain on coefficient of strain rate sensitivity m at $\dot{\varepsilon}=7\times10^{-5}$ s^{-1}

The coefficient of strain rate sensitivity tends to gradually decrease with strain below and above the incipient melting point (Fig. 7). There exists a correlation between the m value (Fig. 7) and the shape of the $\sigma-\varepsilon$ curves (Fig. 4). Steady state flow occurs at $m>0{\cdot}3$; a decrease in the m coefficient to values less than ~0·3 leads to the establishment of strain hardening. This transition occurs at true strains of ~0·7 and ~1·7 at 550°C and 590°C, respectively.

MICROSTRUCTURAL EVOLUTION

The microstructural evolution of the modified 6061 alloy was studied under both static (grip section) and dynamic (gauge section) annealing in the temperature range 475–600°C and $\dot{\varepsilon}=2{\cdot}8\times10^{-4}$ s^{-1}. Grain sizes observed after static annealing L_s dynamic annealing L_d and the grain aspect ratio AR, are summarised in Table 2. In the temperature range 475–500°C there exists significant static grain growth and, in fact, at 500°C, the mean grain size is larger by a factor of 1·6 in comparison with the thremomechanically processed material. In the temperature range 500–570°C, limited additional static grain growth is observed. The mean grain size of about 20 μm remains unchanged with increase of the temperature to 590°C. Thus, the 6061 Al exhibits moderately large superplastic elongation in the entirely solid state, and superior superplastic properties in the semisolid state at 590°C despite the initial grain size of ~20 μm. At 600°C, extensive static grain growth occurs. It is worth noting that the size and volume fraction of Al_3Zr dispersoids remain virtually unchanged under static annealing even at 590°C for 14 h.

Volume fraction and mean size of dispersoids observed after static annealing are summarised in Table 3. At 590°C, static annealing leads to a slight decrease in the size of Al_3Zr dispersoids and Mg_2Si particles (Table 3). It is apparent that this can be caused by partial dissolution of these particles. A decreased volume fraction of dispersion particles at 590°C compared with the initial state (Table 3) supports this assumption.

Remarkable grain growth during superplastic deformation was found only at $T\geqslant570$°C (Table 2). At $\varepsilon\leqslant1{\cdot}1$, insignificant grain elongation along the tension axis was observed (Figs. 8*a* and 8*c*, Table 2). The grain aspect ratio, defined as the ratio of the grain dimension in the longitudinal direction to that in the transverse direction, is 1·24±0·06. This value is typical for standard superplastic alloys with high contributions of grain boundary sliding (GBS) to the total elongation.[5–7,18–20] In the temperature range 525–570°C the grains elongate extensively along the tension axis during subsequent deformation up to failure (Figs. 8*b* and 8*d*, Table 2) because of dislocation creep.[18–20] It is apparent, that slight grain elongation is associated with steady state flow and $m>0{\cdot}4$; high grain elongation is associated with secondary strain hardening and $m\leqslant0{\cdot}33$ (Figs. 4, 7 and 8, Table 2). The decreasing m coefficient with strain (Fig. 7) is associated with concurrent grain elongation and growth leading to the termination of superplastic deformation and establishment of secondary strain hardening. It is worth noting that TEM observation of samples strained at 590°C and $\dot{\varepsilon}=2{\cdot}8\times10^{-4}$ s^{-1} to $\varepsilon=0{\cdot}7$ did not reveal any remarkable effect of superplastic deformation on mean size and volume fraction of dispersion particles.

The average size of cavities A, coefficient of cavity aspect ratio CAR, and porosity volume fraction V in the 6061 alloy after superplastic deformation are presented in Table 4. It is seen that the volume fraction of porosity measured by the buoyancy method is higher than that determined by the metallographic technique. At $T\leqslant570$°C, large cavities were observed to grow along the tensile direction and had an irregular, jagged shape (Figs. 8*a* and 9*a*, Table 4), suggesting plasticity controlled cavity growth. Large, irregular cavities account for ~20% by number, but their volume fraction is ~60% at $\varepsilon=1{\cdot}1$ (Fig. 9*a*) and tends to increase with strain. Another type of cavitation is fine cavities exhibiting equiaxed shape (Figs. 8*a*), which suggests diffusion

Table 2 Grain size in 6061 alloy after superplastic deformation to $\varepsilon=1{\cdot}1$ and to failure at $\dot{\varepsilon}=2{\cdot}8\times10^{-4}$ s^{-1}

	Just before failure				$\varepsilon=1{\cdot}1$	
T, °C	ε_{AE} ,%/ε_{TAE}/ τ_{ET},h	L_s, μm	L_d, μm*	AR	L_d, μm*	AR
475	200/1·1/2·9	12	14·2/12	1·18	13·6/11·6	1·17
500	240/1·22/3·1	17·6	21·7/16	1·36	18/13·7	1·3
525	280/1·34/3·6	18·8	24·7/16·8	1·45	18·5/14·7	1·26
550	380/1·57/4·6	20·5	22·2/15·6	1·42	21·6/18	1·2
570	580/1·92/6·6	21·9	29/19·7	1·47	25·2/21·4	1·18
590	1300/2·64/14	21·3	49/30	1·63	32/26	1·23
600	15/0·14/1	26·4	26·5/23	1·15	–	–

ε_{EA}=local strain in area examined; ε_{TEA}=true local strain in area examined; τ_{ET}=the period of equivalent exposure time.
*Grain sizes measured in tension and transverse directions in the gauge section of the deformed samples are given to the left (resp. right) of the oblique.

Table 3 Zener drag pressure P_Z calculated for Al_3Zr and Mg_2Si particles and their average size D_p and volume fraction V for samples after homogenisation and subjected to the TMP followed by static annealing at 590°C for 4 h

	Initial state*	Static annealing at 590°C*
D_p, nm	32·5/158	24·4/140
V, %	0·59/1·38	0·48/1·25
P_Z, N m^{-2}	$1{\cdot}6\times10^5/9{\cdot}0\times10^4$	$1{\cdot}8\times10^5/7{\cdot}0\times10^4$

*Figure to the left of the oblique denotes Al_3Zr dispersoids, and that to the right denotes Mg_2Si particles.

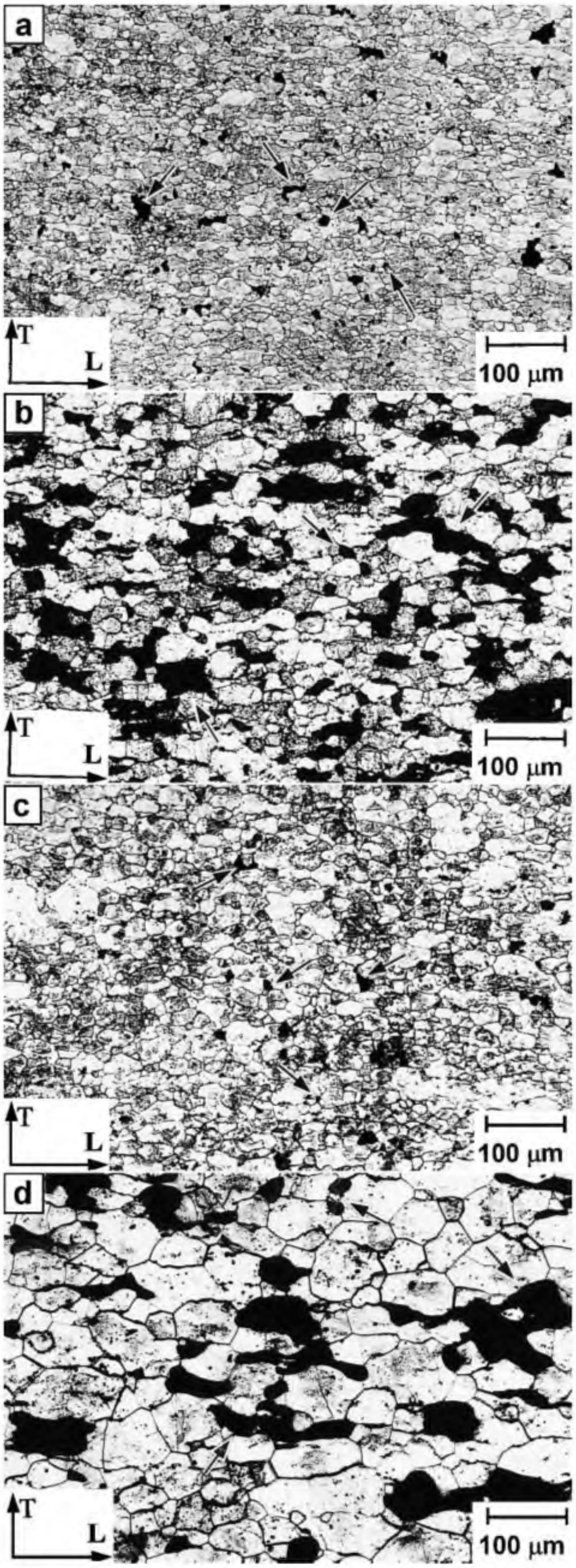

a 550°C, $\varepsilon=1{\cdot}1$; *b* 590°C, $\varepsilon=1{\cdot}1$; *c* 550°C, $\varepsilon=1{\cdot}6$; *d* 590°C, $\varepsilon=2{\cdot}64$

8 Microstructure after superplastic deformation at $\dot{\varepsilon}=2{\cdot}8\times10^{-4}$ s^{-1}: arrows indicate cavities visible as black areas

controlled growth. With increasing strain, the large cavities grow extensively and elongate along the tensile direction (Fig. 8*b*, Table 4). In addition, small cavities are formed. As a result, in the samples pulled to failure, an increasing volume fraction of porosity was observed despite a decrease in average cavity size. Thus, plasticity controlled cavity growth provides a major contribution to the increasing volume fraction of porosity with strain resulting in sample fracture below the incipient melting temperature. At a fixed strain of 1·1, the cavity volume fraction V and mean cavity size tend to increase with increasing temperature for $T\leqslant570$°C.

At 590°C, large cavities with irregular shape were rarely observed (Figs. 8*c*, 9*b*). As a result, at $\varepsilon=1{\cdot}1$, the mean size of cavities and their volume fraction are remarkable less than that at 570°C (Fig. 9*b*, Table 4). It is important to note that this fact is caused mainly by a drop in the number of large cavities (Fig. 9*b*). As a result, the CAR tends to approach unity and average cavity size tends to increase with strain (Table 4). These facts strongly suggest that cavity growth is dominated by a diffusion controlled mechanism. Thus, incipient melting significantly enhances the compatibility of plastic deformation, and diffusion controlled cavity growth provides a significant contribution to the increasing volume fraction of porosity. This diffusion controlled cavity growth occurs slowly, and, as result, a critical volume fraction of porosity, which results in sample fracture, is attained at higher strain than at 570°C. At higher strain, the formation of large cavities, elongated along the tension axis, was detected (Fig. 8*d*). This type of cavitation results in sample fracture. Notably, the cavity size in samples pulled to failure at 590°C is remarkably higher than that at lower temperatures. The volume fraction of porosity is essentially similar at all temperatures. It seems that fracture occurs when the cavity fraction reaches a critical value.

Discussion

The Zr addition to the 6061 alloy resulted in the formation of Al_3Zr type dispersion particles. These dispersoids, which are characterised by low solubility during static annealing even in the partially melted state at $T\leqslant590$°C, effectively pin grain boundaries. To evaluate the effect of the Zr addition on grain stabilisation under static annealing the Zener drag pressure was evaluated according to the procedure described by Nes *et al.*[21] It is known that calculation of the total restraining force originating from the particles distinguished by shape and size distribution on a migrating

Table 4 Average cavity size A and porosity volume fraction V for the modified 6061 alloy deformed at $\dot{\varepsilon}=2{\cdot}8\times10^{-4}$ s^{-1} to $\varepsilon=1{\cdot}1$ and just before failure at various temperatures

	Just before failure				$\varepsilon=1{\cdot}1$		
T, °C	ε_{EA}, %/ ε_{TEA}	A, μm*	CAR	V†, %	A, μm*	CAR	V†, %
475	200/1·1	11·9/8·4	1·42	8·1/–	16·8/12·4	1·36	0·15/0·4
500	240/1·22	17·9/12·5	1·43	14·5/26	14·4/12·4	1·14	0·28/1·8
525	280/1·34	13·1/9·5	1·38	11·8/24·6	14·8/11·7	1·27	0·53/2·7
550	380/1·57	15·5/11·9	1·3	12·1/22·9	22·1/15·1	1·46	0·83/2·5
570	580/1·92	15·7/9·9	1·59	9·3/18·4	22·6/18·7	1·22	1·21/3·0
590	1300/2·64	26·4/16·1	1·64	12·1/19·4	17·9/15·5	1·16	0·61/1·2
600	15/0·14	4·9/4·1	1·20	0·5	–	–	–

ε_{AE}=local strain in area examined; ε_{TAE}=true local strain in area examined.

*Figure to the left of the oblique is the tension direction and that to the right is the transverse direction.

†Figure to the left of the oblique is obtained by metallographic technique and that to the right is obtained by the buoyancy method.

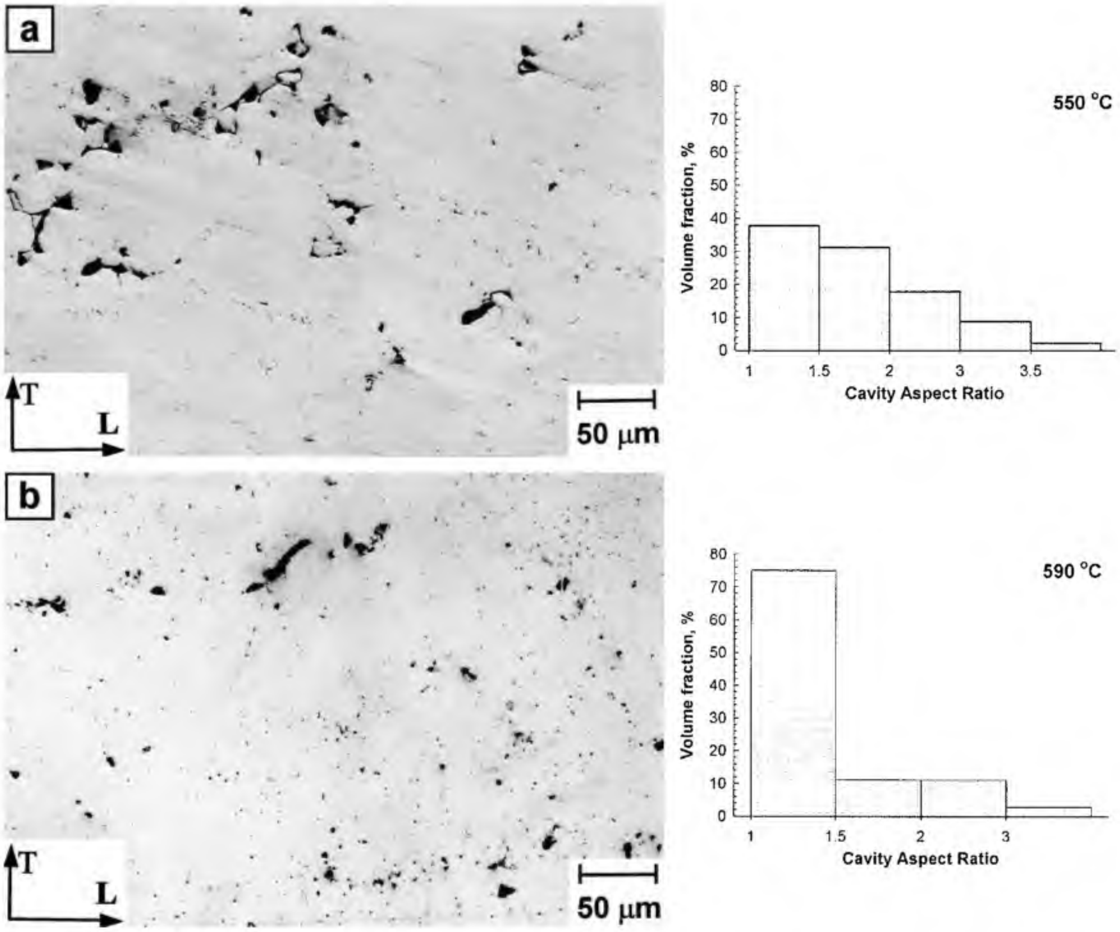

a 550°C; *b* 590°C

9 Microstructure observation at $\dot{\varepsilon}=2\cdot8\times10^{-4}$ s^{-1}, $\varepsilon=1\cdot1$: plots represent dependence of porosity volume fraction on cavity aspect ratio

grain boundary is a very difficult task, which has not been solved yet.[21] The Zener drag pressure P_Z was evaluated for Al_3Zr and Mg_2Si particles, separately, assuming a random distribution of particles by using following expression[21]

$$P_Z = \frac{3}{2} f \frac{\gamma}{R} \qquad (4)$$

where f is volume fraction of particles, γ is grain boundary energy taken as 0·3 N m^{-1} (Ref. 22), and R is radius of particles. Equation (4) was used presuming that all particles exhibit equiaxed shape. In this case, the accuracy of the calculation of Zener drag originating from the Mg_2Si particles is about 30%[23] taking into account that the values of Mg_2Si particle aspect ratio (defined as the ratio of the highest dimension of a particle to that in the perpendicular direction) lies in the range 1·4 to 2. Calculations of the drag pressure are summarised in Table 3. It is seen that the Zener pressure originating from Al_3Zr dispersoids is slightly higher than that originating from Mg_2Si particles. Increasing temperature results in a slightly increased value of restraining force originating from Al_3Zr dispersoids due to the decreased size of these particles. Thus, the formation of Al_3Zr dispersoids enhances the Zener drag pressure, especially in the partially melted state.

As a result, moderately fine grains are remarkably stable in the temperature interval 500–590°C under superplastic deformation conditions, and the modified 6061 Al, subjected to two step recrystallisation TMP, can exhibit moderate superplastic ductilities below the incipient melting temperature, and superior superplastic properties above ~575°C. In the solid state, increasing the temperature of superplastic deformation enhances superplastic elongations. However, this occurs with a slight increase in the optimal strain rate for superplasticity. Therefore, only relatively low forming rates may be used for blow forming of 6061 alloy in the solid state as well as in the partially melted state.

The extraordinary enhancement of superplastic elongations above the incipient melting temperature is attributed to lower cavitation levels. At ~575°C, a small amount of liquid phase is formed, as a thin layer, at grain boundaries and particularly grain triple junctions.[24–28] This liquid phase plays the role of a 'helper' in GBS accommodation providing high compatibility of plastic deformation between neighbouring grains.[24] However, the efficiency of the liquid phase in enhancing the superplastic characteristics is strongly dependent on the corresponding strain rate. At $\dot{\varepsilon}\geqslant 1\cdot4\times10^{-3}$ s^{-1}, partial melting leads to decreased tensile elongation. As a result, no significant increase in the optimal strain rates for superplastic deformation is observed. It is apparent that increasing the optimal strain rate region for superplasticity to higher strain rates at 590°C, in comparison with 550°C (Fig. 5), occurs due to increasing temperature. Therefore, partial melting does not result in superplastic elongation at higher strain rates. The formation of a small amount of liquid phase can only enhance superplastic elongation in the entirely solid state.

Conclusions

A 0·15%Zr+0·7%Cu modified 6061 aluminium alloy can be thermomechanically processed through a simple procedure into a uniform fine grained (~ 11 μm) structure. The superplastic properties of the modified 6061 aluminium alloy were examined by tensile tests at temperatures ranging from 475 to 600°C, and at strain rates ranging from $1{\cdot}4\times10^{-5}$ to $2{\cdot}8\times10^{-3}$ s^{-1}. In the solid state, it was shown that the modified 6061 alloy exhibits superplasticity at $\dot{\varepsilon}=2{\cdot}8\times10^{-4}$ s^{-1} with the highest elongation to failure (580%) at 570°C. In the partially melted state, the maximum tensile elongation of 1300% was observed at 590°C. Significant increases in elongation result from the formation of a small amount of liquid phase in the modified 6061 alloy. The ductility of the alloy at 590°C was dependent upon strain rate, and it decreased sharply from 1300% at $2{\cdot}8\times10^{-4}$ s^{-1} to 250% at $1{\cdot}4\times10^{-3}$ s^{-1} despite a high measured m value.

Acknowledgements

This work was performed under the auspices of the US Department of Energy by LLNL under contract No. W–7405–Eng–48.

References

1. T. G. NIEH, R. KAIBYSHEV, F. MUSIN and D. R. LESUER: Proc. Conf. on 'Superplasticity and superplastic forming' (ed. A. Ghosh *et al.*), 137–144; February 1998, San-Antonio, USA, TMS.
2. E. KOVACS-CSETENY, T. TORMA, T. TURMEZEY, N. Q. CHINH, A. JUHASZ and I. KOVACS: *J. Mater. Sci.*, 1992, **27**, 6141–6145.
3. L. P. TROEGER and E. A. STARKE JR: *Mater. Sci. Eng. A*, 2000, **A277**, 102–113.
4. L. P. TROEGER and E. A. STARKE JR: *Mater. Sci. Eng. A*, 2000, **A293**, 19–29.
5. T. G. NIEH, J. WADSWORTH and O. D. SHERBY: 'Superplasticity in metals and ceramics', 1996, New York, Cambridge University Press.
6. O. A. KAIBYSHEV: 'Superplasticity of alloys, intermetallides, and ceramics', 1992, Berlin, Springer-Verlag.
7. J. PILLING and N. RIDLEY: 'Superplasticity in crystalline solids', 1989, London, The Institute of Metals.
8. C. A. LAVENDER, J. S. VETRANO, M. T. SMITH, S. M. BRUEMMER and C. HAMILTON: *Scr. Mater.*, 1994, **30**, 565–568.
9. N. E. PATON and C. H. HAMILTON: US Patent no. 4,092,181, 30 May, 1978.
10. A. WERT, N. E. PATON, C. H. HAMILTON and M. W. MAHONEY: *Metall. Trans. A*, 1981, **12A**, 1267–1276.
11. F. J. HUMPHREYS and M. HATHERLY: 'Recrystallisation and related annealing phenomena'; 1996, Oxford, Pergamon Press.
12. F. J. HUMPHREYS: *Acta Metall.*, 1977, **25**, 1323–1344.
13. W. CUBBERLY, H. BAKER, D. BENJAMIN, P. UNTERWEISER, C. KIRKPATRIC, V. KNOLL and K. NIEMAN: 'Metals handbook, 9th Edition. Vol. 2 Properties and selection: nonferrous alloys and pure metals', 1979, Metals Park, OH, ASM.
14. KAISER ALUMINIUM AND CHEMICAL CORPORATION, CENTER FOR TECHNOLOGY: 'Metallography handbook for 6061Al'; 1992, Pleasanton, CA.
15. R. KAIBYSHEV, T. SAKAI, F. MUSIN, I. NIKULIN and H. MIURA: *Scr. Mater.*, 2001, **45**, 1373–1380.
16. R. KAIBYSHEV, I. KAZAKULOV, D. GROMOV, F. MUSIN, D. R. LESUER and T. G. NIEH: *Scr. Mater.*, 2001, **44**, 2411–2417.
17. M. MABUCHI and K. HIGASHI: *Mater. Trans. JIM*, 1994, **35**, 399–405.
18. P. A. FRIEDMAN and A. K. GHOSH: *Metall. Trans. A*, 1996, **27A**, 3827–3839.
19. F. LI, D. H. BAE and A. K. GHOSH: *Acta Mater.*, 1997, **45**, 3887–3895.
20. D. H. BAE and A. K. GHOSH: *Acta Mater.*, 2000, **48**, 1207–1224.
21. E. NES, N. RYUM and O. HUNDER: *Acta Metall.*, 1985, **33**, 11–22.
22. L. F. MURR: 'Interfacial phenomena in metals and alloys', 1975, Reading, MA, Addison-Wesley.
23. W. B. LI and K. E. EASTERLING: *Acta Metall. Mater.*, 1990, **38**, 1045–1052.
24. M. MABUCHI and K. HIGASHI: *Philos. Mag. Lett.*, 1994, **70**, 1–5.
25. J. KOIKE, M. MABUCHI and K. HIGASHI: *Acta Metall. Mater.*, 1995, **43**, 199–206.
26. K. HIGASHI, T. G. NIEH and J. WADSWORTH: *Acta Metall. Mater.*, 1995, **43**, 3275–3282.
27. K. HIGASHI, T. G. NIEH, M. MABUCHI and J. WADSWORTH: *Scr. Metall. Mater.*, 1995, **32**, 1079–1084.
28. J. KOIKE, K. MIKI, K. MARUYAMA and H. OIKAWA: *Philos. Mag. A.*, 1998, **78**, 599–614.